Title
Spectral imaging at high definition and high speed in the mid-infrared.

Journal
Science advances, 8(46)

ISSN
2375-2548

Authors
Knez, David
Toulson, Benjamin W
Chen, Anabel
et al.

Publication Date
2022-11-01

DOI
10.1126/sciadv.ade4247

OPTICS

Spectral imaging at high definition and high speed in the mid-infrared

David Knez[1], Benjamin W. Toulson[1], Anabel Chen[1], Martin H. Ettenberg[2], Hai Nguyen[2], Eric O. Potma[1], Dmitry A. Fishman[1]*

Spectral imaging in the mid-infrared (MIR) range provides simultaneous morphological and chemical information of a wide variety of samples. However, current MIR technologies struggle to produce high-definition images over a broad spectral range at acquisition rates that are compatible with real-time processes. We present a novel spectral imaging technique based on nondegenerate two-photon absorption of temporally chirped optical MIR pulses. This approach avoids complex image processing or reconstruction and enables high-speed acquisition of spectral data cubes (xyω) at high-pixel density in under a second.

INTRODUCTION

In spectral imaging, each pixel in a two-dimensional (xy) image is expanded along the optical frequency (ω) axis, yielding an information-rich data cube (xyω) of both spatial and spectral information. When realized in the mid-infrared (MIR) spectral region, spectral imaging allows direct spatial differentiation of chemical composition, providing an indispensable tool for many applications in chemical, medical, and bio-related fields. MIR spectral imaging has been used to great effect in label-free histopathological imaging (*1*, *2*), standoff detection of materials (*3*–*6*), gas analysis (*7*), and environmental surveying (*8*). However, a broader utilization of the technique for applications that require both high-speed and high-definition imaging capabilities has remained challenging. Conventional interferometric Fourier transform infrared (FTIR) methods are generally too slow for rapid analysis or in situ observations of real-time processes (*9*). In this context, there is a need for MIR spectral imaging technologies that combine high-pixel density mapping with high acquisition and image processing speed.

MIR imaging historically suffers from technological limitations associated with detection of infrared radiation. Traditional detection approaches are based on the linear absorption of MIR light by small-bandgap semiconductors, such as mercury cadmium telluride (MCT) or indium antimonide (InSb). Such single element or matrix arrays are susceptible to thermal noise and thus require active cooling, often down to cryogenic temperatures. In addition, for arrayed detectors, there is a trade-off between pixel density and the overall response time of the detector assembly. Whereas readout times of small focal plane arrays (up to 128 × 128) can be fast, the frame rate of larger MIR-sensitive arrays is typically too slow for high-speed imaging applications (*9*). Moreover, wide-field FTIR imaging uses a low-brightness broadband source and necessitates an interferometric scan plus subsequent processing to reconstruct the MIR absorption spectrum, which can slow down the overall acquisition process. Recent approaches based on quantum cascade lasers (QCLs) benefit from higher brightness and an alternative spectral scanning scheme that involves rapid sweeping of a narrow spectral window (*1*, *2*). For instance, MIR spectral imaging covering a full spectral octave with four synchronized QCL lasers has been achieved, enabling hyperspectral data cube acquisition within ~3 s using a focal plane array of 128 × 128 pixels (*2*). Given the limited number of pixels of the array, mosaicking over a larger sample area was needed to collect images of higher definition, extending the overall collection time to several minutes.

A new cohort of MIR imaging approaches has been developed to address the aforementioned limitations of arrayed MIR detectors. These methods make use of a conversion step through which information encoded in the MIR part of the spectrum is transferred to the visible or near-IR (NIR) range of the spectrum, where more mature large-bandgap semiconductor technology can be used. Such a frequency conversion step can be realized in a variety of ways. For instance, several approaches use the nonlinear properties of the sample material itself (*10*–*15*). Other methods use an external nonlinear medium to either reconstruct the image through nonlinear interferometry of entangled photons (*16*, *17*) or, alternatively, via direct upconversion of MIR light through a $\chi^{(2)}$-mediated parametric process (*18*–*20*). In this fashion, MIR images have been collected in as little as 2.5 ms per frame using upconversion in wide-field imaging mode (*21*). Although upconversion enables fast monochromatic imaging, the need for phase-matching adds complexity in both image reconstruction and spectral data acquisition, which can limit a flexible implementation of spectral imaging over a broad bandwidth.

Another conversion method exploits the intrinsic optical nonlinearity of the detector material itself. This detection principle is based on a $\chi^{(3)}$-mediated nonlinear process, namely, nondegenerate two-photon absorption (NTA) (*22*–*24*). In our previous work, we have used NTA in large-bandgap semiconductor materials to directly detect MIR radiation on the chip of visible or NIR cameras (*25*–*27*). This approach allowed us to collect chemically selective MIR images with a megapixel indium gallium arsenide (InGaAs) camera at 500-Hz frame rates. Whereas NTA enables fast MIR imaging with high definition, this principle has not yet been used for spectral imaging. In the current work, we introduce a spectral scanning strategy that takes advantage of the NTA imaging conditions. Using temporally chirped MIR pulses and a short NIR gate pulse, we show that MIR spectral data cubes (xyω) over a spectral

[1]Department of Chemistry, University of California, Irvine, Irvine, CA 92697, USA. [2]Princeton Infrared Technologies Inc., 7 Deerpark Dr. Suite E, Monmouth Junction, NJ 08852, USA.
*Corresponding author. Email: dmitryf@uci.edu

range of >400 cm^{-1} can be acquired in under 1 s with a >1-megapixel (Mpx) InGaAs camera. Without the necessity for image processing or reconstruction, this approach has the potential for true video-rate hyperspectral data acquisition of live processes, enabling rapid data acquisition in all four dimensions, i.e., a (xyωt) hypercube.

RESULTS

Our high-speed spectral imaging technique leverages the broad spectral width of an ultrashort MIR pulse, as illustrated in Fig. 1. Consider first a MIR pulse with a temporal width of 40 fs that is bandwidth limited. In the frequency domain, such a pulse manifests itself with a constant spectral phase, as can be inferred from a simple Fourier transformation (see the Supplementary Materials). In the time-frequency plot of Fig. 1A, the constant spectral phase is associated with a narrow temporal distribution of the different frequency components in the pulse. When the bandwidth-limited pulse traverses a sample, for instance, a thin layer of polystyrene, its spectrum is modified because of the linear absorption of light by the polymer (Fig. 1A). The pulse spectrum now shows narrow spectral features in its otherwise broad spectral profile. In the time domain, the narrow imprints in the MIR pulse spectrum produce almost invisible modification to the temporal profile, most notably a decrease of the overall intensity and the introduction of an extremely shallow pedestal, as shown in Fig. 1B. The NTA signal is obtained by temporally overlapping the MIR pulse with a short NIR gate pulse on the detector. If the gate pulse is scanned in time relative to the MIR pulse, the convolution results in a profile that lacks clearly resolved features related to the MIR spectral imprints.

The situation is different if a linear chirp is applied to the MIR pulse. The time-frequency plot in the inset of Fig. 1C shows the original MIR pulse that has been linearly chirped to a temporal width of 4.5 ps, corresponding to a quadratic spectral phase (see the Supplementary Materials). Different frequency components now have their maximum intensity at different moments in time. Whereas the spectral phase has no direct effect on the absorption imprints in the pulse's power spectrum that is observed in the frequency domain (Fig. 1C), it has a profound effect on the MIR pulse in the time domain. As shown in Fig. 1D, the time-resolved MIR pulse shows variations that mimic the spectral features in the frequency domain. In the case of linear chirp, there is a linear relationship between the time and frequency axis, allowing a direct reading of the spectrally encoded information in the time domain. Using the gated principle of NTA detection, the MIR pulse spectrum can be directly accessed through a rapid scan of the MIR and gate-relative time delay, i.e. a cross-correlation. Note that for sufficiently broadened MIR pulses, the spectral information is largely unaffected by

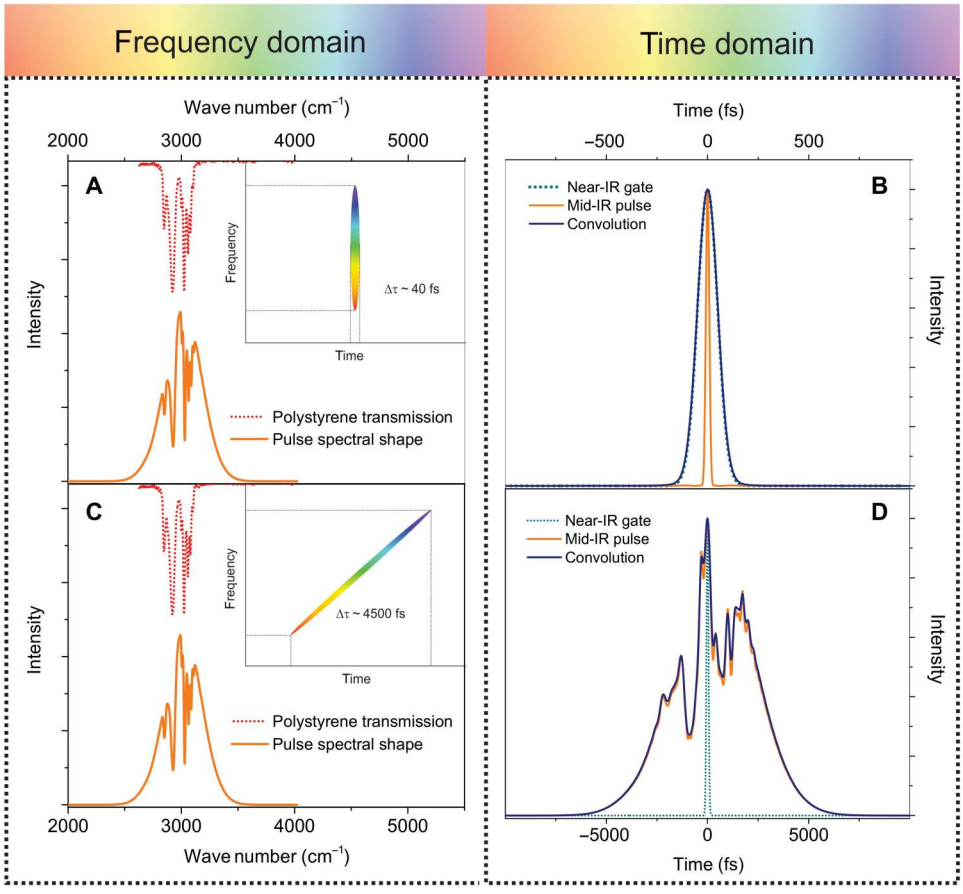

Fig. 1. Visualized concept of chirped pulse–NTA (CP-NTA). The broad pulse spectrum is modified because of linear absorption of light by the sample (**A** and **C**). Inset shows a time-frequency plot of the MIR pulse in the absence or presence of linear chirp. (**B** and **D**) The resulting pulse shape in the time domain without (B) and with (D) introduction pulse chirp. Dark blue lines illustrate the convolution between the MIR and gate pulses.

the convolution with the gate pulse. The use of chirped pulses for encoding spectral information in time-domain signals has been demonstrated for various forms of spectroscopy (*28*) and has recently been an important approach for achieving high spectral resolution in coherent Raman scattering microscopy with broad bandwidth pulses (*29*, *30*). NIR chirped pulses have also been used to upconvert MIR signals to the visible range with the aid of nonlinear crystals (*31*, *32*). Here, we show that this principle can be extended to MIR spectral imaging through NTA by chirping the MIR pulse instead.

A schematic of the experimental implementation of the chirped pulse NTA (CP-NTA) imaging technique is shown in Fig. 2. We use an ultrashort MIR pulse centered at 3.33 μm (3000 cm^{-1}) that is stretched by a 15-cm-long Si rod (see Materials and Methods). The stretched pulse is subsequently passed through the sample and imaged with two CaF_2 lenses onto a >1.3-Mpx lattice matched $In_{0.53}Ga_{0.47}As$ camera chip (0.734 eV, 1690-nm bandgap). The NIR gate pulse is centered at 1900 nm (5263 cm^{-1}) with a temporal width of 116 fs. The gate pulse passes through a delay stage before it is coincident with the MIR pulse on the detector chip. Note that the camera chip is covered with a fused silica protective window, which substantially-attenuates the MIR beam (0.75 optical density at 3000 cm^{-1}; see fig. SF3). The intensity ratio between the MIR and the gate pulse is chosen such that the linear NTA signals are on par with the degenerate two-photon absorption (DTA)) signal induced by the gate pulse. This DTA signal forms a constant background that does not affect the spectral information nor markedlyly change the detection dynamic range. More details on the experimental parameters can be found in the Supplementary Materials (see table S1).

The linear relation between the time and frequency axis in CP-NTA relies on the successful application of linear chirp. This can be achieved with MIR transparent materials that exhibit sufficient group velocity dispersion with limited higher-order dispersion. We have found that such can be realized with a Si rod. The MIR pulse spectrum is shown in Fig. 3A, indicating a full width at half maximum (FWHM) of 360 cm^{-1}, as measured using a grating-based spectrometer equipped with a single-pixel MCT detector (~20 s per spectral point; see Materials and Methods). This spectrum supports a bandwidth-limited temporal width of 40 fs. Figure 3B depicts the NTA signal on the camera as a function of the MIR-gate delay time. We can find the temporal width of the MIR pulse from the NTA cross-correlation of the MIR and gate pulses. In the absence of the Si rod, the MIR pulse duration is found as 160 fs, which is longer than the minimum width of 40 fs because of residual dispersion by the optical elements in the setup. Upon insertion of the Si material in the MIR beam, the NTA cross-correlation is substantiallyly elongated in time, revealing a MIR pulse with a temporal width of 4.5 ps (see also fig. SF4).

When the MIR pulse passes through a 7-μm layer of polystyrene, a frequency-domain measurement reveals a pulse spectrum with narrowband imprints of vibrational absorption lines as is evident from Fig. 3C. The absorption features correspond to the symmetric and asymmetric stretching vibrations of the carbon-hydrogen bonds of polystyrene. Using the chirped pulse this spectral information can also be obtained in the time domain, as shown by the NTA cross-correlation in Fig. 3D. The time-domain measurement was collected using a 16-ms dwell time per spectral bin for a total effective acquisition time of 800 ms. In the current configuration, the available spectral range can be extended to ~530 cm^{-1} for a 1.1-s effective acquisition time per spectral sweep.

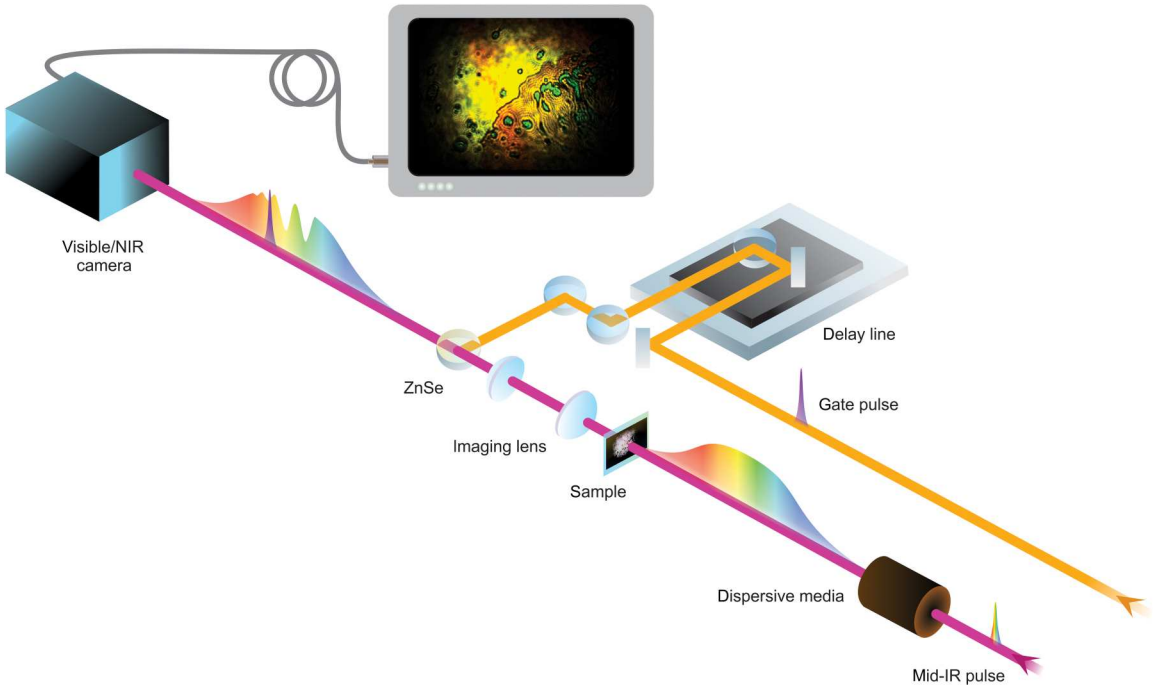

Fig. 2. Schematic of experimental setup. An ultrashort MIR pulse is chirped by propagation through a 15-cm Si rod and spatially overlapped with a temporally short gate pulse on the camera chip. Control of the MIR-gate pulse time delay permits a rapid spectral scan across the MIR pulse spectrum.

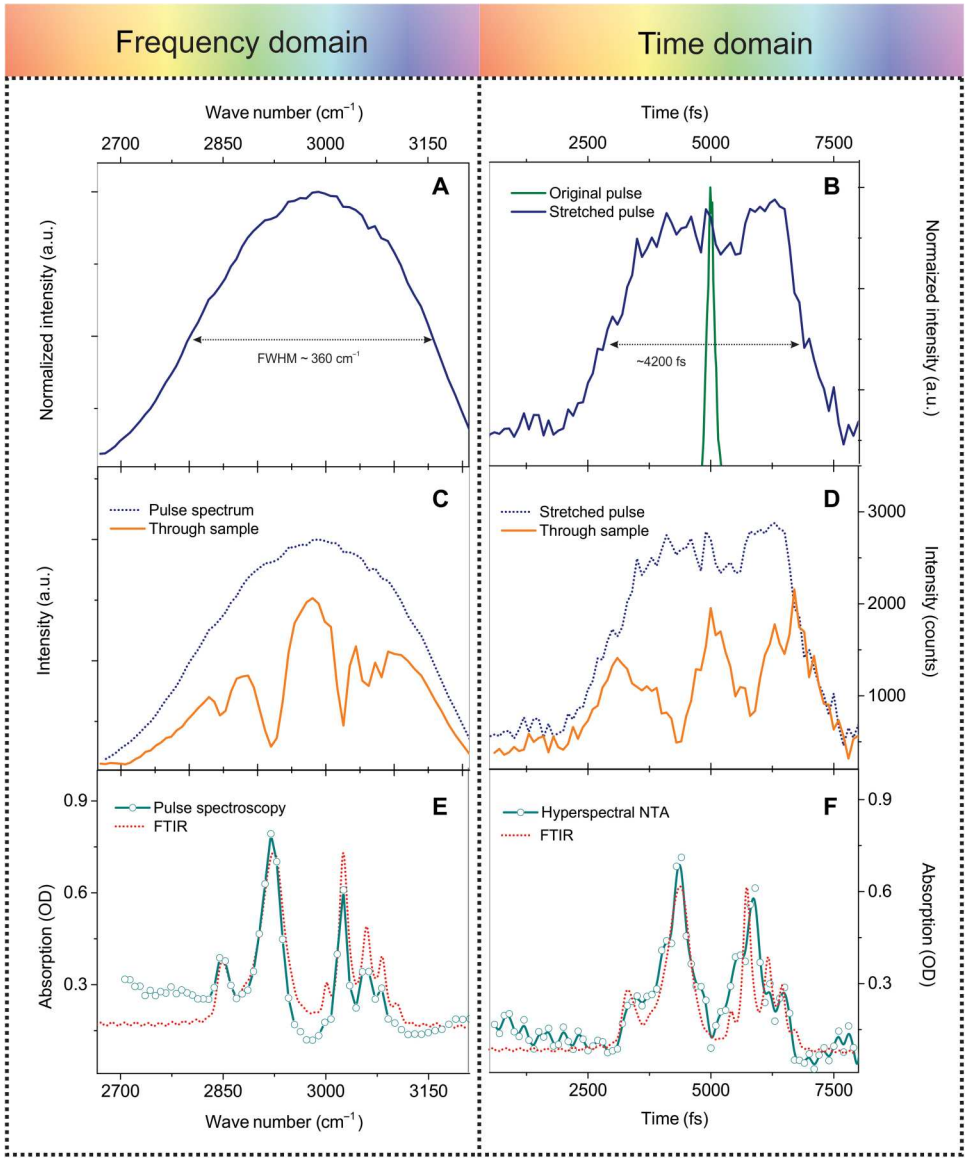

Fig. 3. Demonstration of MIR spectroscopy using CP-NTA. Side-by-side demonstration of spectroscopy on polymer standard (7-μm polystyrene) in frequency domain (spectrometer, left, **A** and **C**) and time domain (CP-NTA, right, **B** and **D**). (**E** and **F**) Retrieved absorption spectra are in good agreement with the polystyrene absorption lines. OD, optical density.

The corresponding MIR absorption spectrum can be derived from the measured pulse spectra, either in the frequency domain (Fig. 3E) or in the time domain (Fig. 3F). Both datasets show good agreement with the signatures in the FTIR spectrum of polystyrene. Using the positions of the polystyrene absorption lines as calibration standards, we determine a chirp rate of $\beta \sim 0.072$ cm^{-1}/fs (see the Supplementary Materials). This corresponds to an instrument response function of ~8.4 cm^{-1}, which spans the frequency window of temporal overlap between the short gate pulse and the chirped MIR pulse. The latter is also confirmed from an analysis of the main polystyrene lines retrieved from CP-NTA. The spectral features at 2923 cm^{-1} (FTIR FWHM = 35 cm^{-1}) and 3025 cm^{-1} (FTIR FWHM = 15 cm^{-1}) yield spectral widths of 38 and 19 cm^{-1}, respectively, after convolution with a Gaussian resolution function of spectral width 8.4 cm^{-1} (see fig. SF5).

The linearity of the temporal chirp of the MIR pulse is important for direct frequency-to-time conversion. To confirm the linear distribution of frequency components, i.e., the linearity of the instantaneous frequency, we perform CP-NTA spectroscopic imaging with pulses of various carrier frequencies ω_0 around the polystyrene absorption bands (fig. SF6). The data show that the line positions and overall absorption spectra remain identical regardless of carrier frequency of the MIR pulse. This observation indicates a good linearity of the instantaneous frequency distribution across the full width of the MIR pulse.

Figure 4 shows an example of unprocessed hyperspectral imaging data for a sample composed of adjacent polymethyl

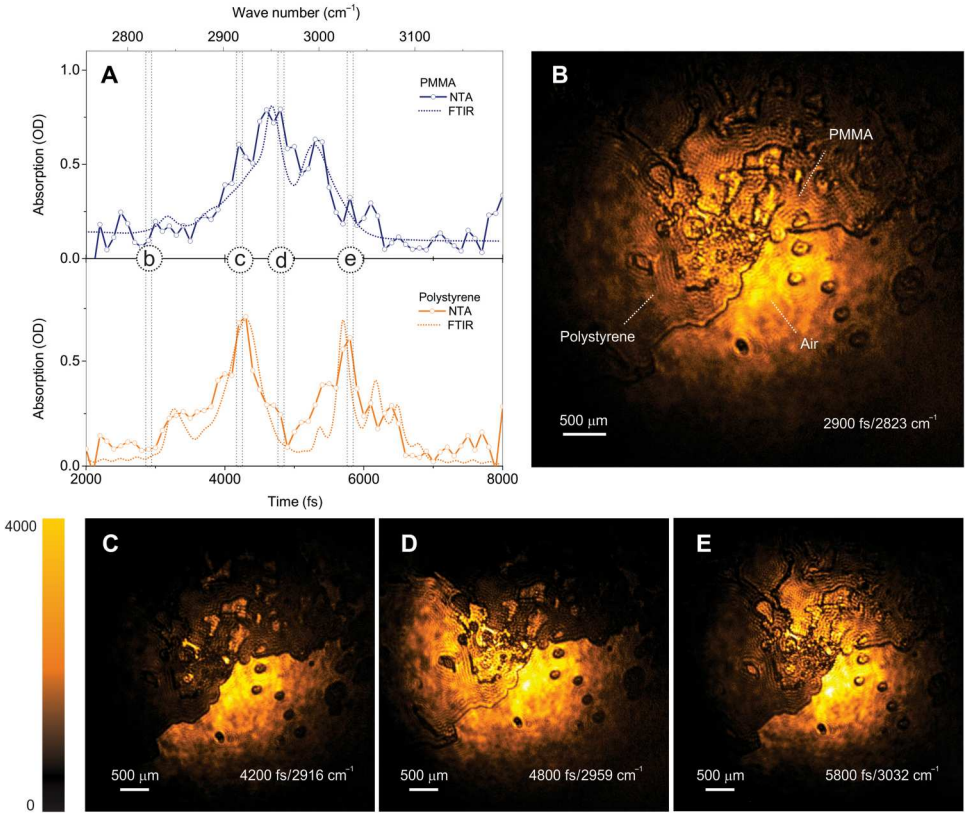

Fig. 4. Unprocessed spectral imaging of polymer samples. (**A**) Polymer absorption spectrum extracted from the hyperspectral data cube. (**B** to **E**) Raw transmission images at different positions in time/spectral domain, directly revealing spatially dependent chemical information in the field of view. Acquisition time is 16 ms per frame/spectral point.

methacrylate (PMMA) and polystyrene layers. These materials feature several distinct absorption lines near 2900 cm^{-1}. When the sampled MIR frequency is tuned to 2823 cm^{-1} (2900 fs in time domain), which is off-resonance for both compounds, both layers appear transparent (point b on Fig. 4, A and B). Upon rapidly scanning the time delay, the polymers appear darker or brighter, following their absorption spectral profile. Figure 4 (C to E) shows several unprocessed frames from the hyperspectral data cube, revealing clear transmission differences between the different materials due to their absorption profiles.

To reduce the dimensionality of the hyperspectral data stack and demonstrate chemical differentiation, we select two images from the data cube where one polymer appears transparent, while another exhibits strong absorption and vice versa (green and red spectral points; Fig. 5, A and C). These two frames are represented as the red (R = 100, G = 0, and B = 0) and green (R = 0, G = 100, and B = 0) channels and color-merged to form the single image. The results are shown in Fig. 5 (B and D), which differentiate the spatial distribution of the two polymers within the field of view. Similarly, Fig. 6 displays reduced dimensionality spectral images of various organic materials and their combinations images through CP-NTA: (A) polystyrene, (B and F) a PMMA/polystyrene structure, (C) ethanol, (D) silicone lubricant (polydimethylsiloxane as main component), and (E) a melted polyethylene flake. The images are composed of two 16-ms frames at two different spectral positions, separated by 72 cm^{-1} in the frequency domain (1 ps separation in time), and represent the on and off resonance positions of a given material. Overlay of the red and green frames then yields an image with chemical contrast.

DISCUSSION

In this work, we have introduced an MIR spectral imaging approach, namely, CP-NTA. This technique takes advantage of the attractive features of NTA-based MIR detection. Chief among these advantages is the ability to collect MIR images at high definition. Unlike the relatively low pixel density matrix of the fastest focal plane arrays, the >1-Mpx detector chips used in NTA offer much improved sampling of the projected MIR image. This high-definition imaging capability does not come at the expense of speed, as NTA benefits from the mature readout technology of visible/NIR cameras, permitting MIR imaging at high frame rates. In addition, the NTA technique is interferometry free and does not rely on phase matching of the MIR and gate pulses, enabling a robust and relatively simple optical setup (*26*, *27*). Furthermore, NTA does not require any image reconstruction or processing for immediate visualization, allowing direct and on-screen observation of fast processes at particular MIR frequencies.

The key advance in this work is the expansion of NTA-based MIR imaging along the frequency dimension. The CP-NTA method uses the inherent gated detection property of the technique and achieves spectral imaging through time-domain detection by simply adding a dispersive material in the MIR beam. Spectral

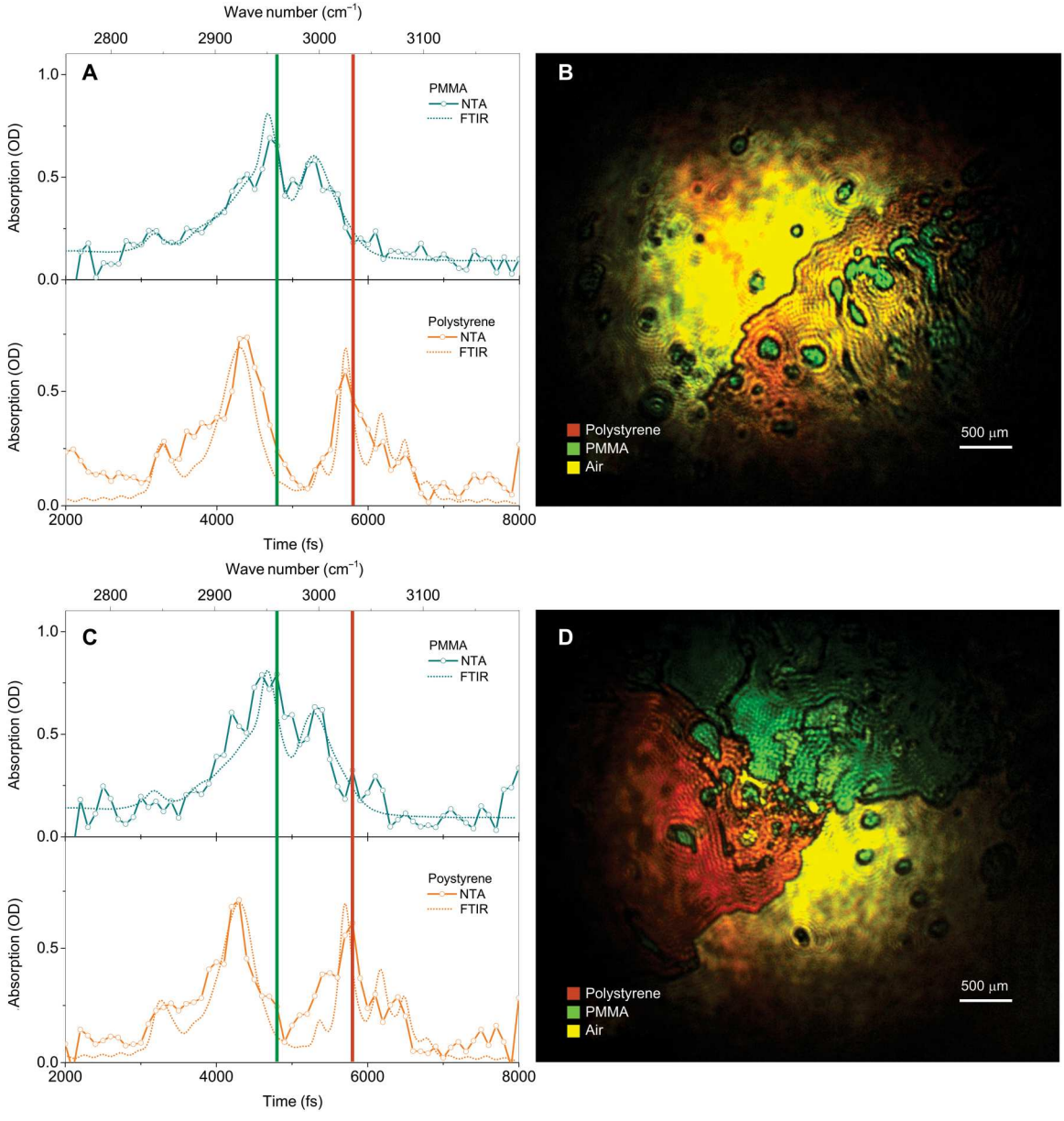

Fig. 5. False color visualization of spectral imaging. Spectral imaging of PMMA/polystyrene films. (**A** and **C**) Spectra of polystyrene and PMMA components obtained by CP-NTA and FTIR. Red and green lines denote spectral position of color channel image. Dimensionality of the hyperspectral data stack is reduced through overlay of red and green color channels measured on and off the absorption resonance of a given polymer. (**B** and **D**) resulting false color spectral image. Effective image acquisition time is ~32 ms (16 ms per frame).

tuning requires scanning a delay line, which can be performed with ease, at high speed, and avoids the need for detuning a light source.

In CP-NTA, each spectral image is acquired in wide-field mode, collecting spectral data at each pixel in a massively parallel fashion. In contrast to laser scanning approaches or wide-field imaging with low-pixel density arrays, which require mosaic stitching to achieve high-definition images, the CP-NTA approach records frames of high pixel number by using >1.3-Mpx camera chips. In this work, we have used a 16-ms image acquisition time for a ~500-kilopixel frame and a >700-px MIR spot diameter. This camera frame rate (62.5 Hz, 16 ms) has been chosen to eliminate signal fluctuations while allowing full matrix array readout. We note that there is room for considerable improvement of the CP-NTA imaging conditions. First, the current CP-NTA signals have been collected without synchronization of the camera to the 1-kHz radiation source, causing additional noise at frame rates beyond 70 Hz. With appropriate electronic synchronization and a more compact source detection arrangement, the MIR acquisition rate for the used camera can be easily increased to 100 Hz for the full 1280 × 1024 window. Second, the current experiments result in only 5 fJ per camera pixel at MIR pulse maximum (fig. SF4). Similar experiments carried out at 100 kHz or higher will significantly improve

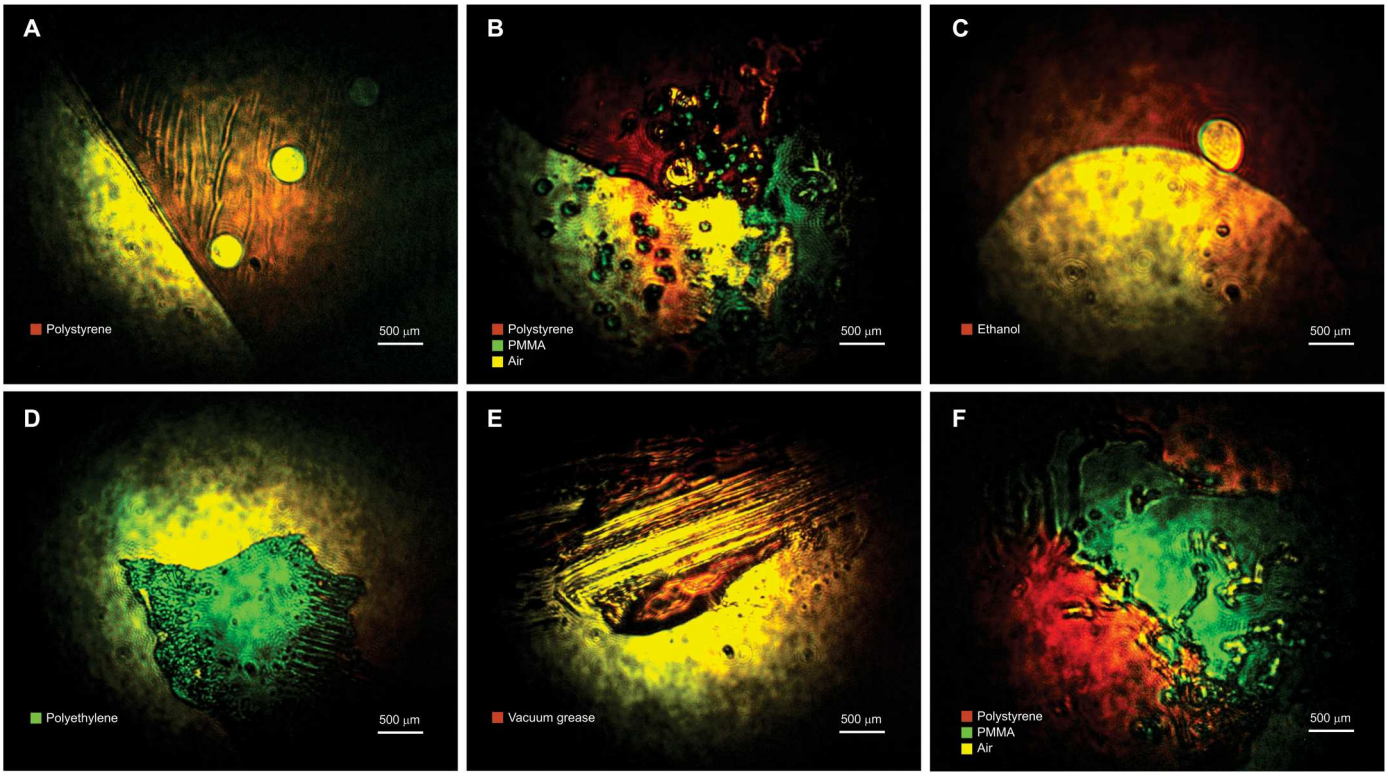

Fig. 6. Spectral images of chemical matrices. Spectral imaging of various materials and material combinations: (**A**) polystyrene, (**B** and **F**) PMMA/polystyrene hybrids, (**C**) ethanol, (**D**) polyethylene, and (**E**) silicone lubricant (polydimethylsiloxane). Effective image acquisition time 32 ms (16 ms per frame).

the detection limits and dynamic range, reaching detection sensitivities of only a few attojoules or tens of photons of MIR radiation on a single camera pixel.

In the spectral domain, the time-frequency sweep can be carried out in a variety of ways. In this work, we have used spectral imaging over the full spectral range of the MIR pulse, but we have also performed MIR imaging with reduced spectral sampling. For example, the data representation in Figs. 5 and 6 is based on only two spectral frames with a fixed time-frequency separation. The spectral separation of 72 cm^{-1} between these two images (1 ps in time) can be acquired within a few milliseconds or faster. Rapid modulation of the spectral position can, for instance, be achieved by chopping the gate pulse beam with 0.7-mm glass windows at rates exceeding 100 Hz, producing on and off frames for high-speed chemical imaging.

In the present experiments, we have used a motorized linear stage that allows a fine spectral sweep with scanning speeds up to 12,000 cm^{-1}/s with precision of 0.72 cm^{-1} (~170,000 fs/s, 10 fs). Other inexpensive approaches exist for rapidly controlling the time-delay setting and performing rapid delay modulation over ~1.5-mm (10-ps) distances. For example, commercially available travel delay stages allow >20-Hz delay modulation over an extended 15-ps range with 10-fs time delay precision. Some of the concepts used for the recent development of rapid delay lines in coherent Raman scattering (*33*–*35*) can also be translated for use in CP-NTA. We are confident that further development of rapid scanning of the time-frequency axis will render CP-NTA suitable for video-rate hyperspectral data acquisition, in which full (xyω) data cubes can be collected in real time.

MATERIALS AND METHODS

Sample preparation

The polymer samples (polystyrene and PMMA) are placed between two coverslips (170 μm) and melted using a hot plate. During the melting process, the polymer sample is pressed flat by a weight until the desired thickness is reached. The methanol sample is prepared by applying 10 μl of the liquid between two coverslips. The sample is subsequently agitated until bubbles appear. Polyethylene samples are cut and placed between two coverslips. Vacuum grease samples are prepared by smearing a small amount of the substance onto a coverslip.

FTIR experiments

Conventional infrared absorption spectra are measured using a Jasco 4700 FTIR spectrometer in attenuated total reflection (ATR) geometries. For the ATR experiments, the Jasco ATR Pro One accessory equipped with a diamond crystal is used. The spectra are averaged over 40 scans and are acquired with a resolution of 2 cm^{-1}.

Frequency-domain experiments with pulsed radiation

Frequency-domain experiments for pulse characterization and spectroscopy are performed using a grating-based spectrometer (CM110, Spectral Products, 150 grooves/mm) equipped with single-pixel–amplified MCT detector (PDAVJ10, Thorlabs). All spectra have been measured with 10-nm spectral resolution (~11 cm^{-1}).

CP-NTA detection

A 1-kHz amplified femtosecond laser system (Spitfire Ace, Spectra Physics) is used to seed two optical parametric amplifiers (OPA, TOPAS-Prime, Light Conversion). One OPA is used as a source of NIR gate radiation at 1900 nm (0.65 eV). The signal and idler pulses from the second OPA system are used to generate MIR pulses through the process of difference frequency generation in a nonlinear medium. Both MIR and NIR pulses are recombined on a 1-mm-thick ZnSe window, which serves as dichroic mirror, after which the pulses are overlapped on an InGaAs camera chip (1280MVCam, Princeton Infrared Technologies Inc.). Temporal overlap is controlled through an automated delay stage (GTS150, Newport). The MIR imaging system consists of two 100-mm CaF_2 lenses, resulting in a 1:1 imaging system with a numerical aperture of 0.015. All experiments are performed with a fixed NIR irradiance of 240 MW/cm^2 and MIR irradiance 0.25 MW/cm^2 on the camera chip.

Supplementary Materials

This PDF file includes:

Supplementary Text
Table S1
Figs. S1 to S7

REFERENCES AND NOTES

1. N. Kröger, A. Egl, M. Engel, N. Gretz, K. Haase, I. Herpich, B. Kränzlin, S. Neudecker, A. Pucci, A. Schönhals, J. Vogt, W. Petrich, Quantum cascade laser–based hyperspectral imaging of biological tissue. *J. Biomed. Opt.* **19**, 111607 (2014).
2. K. Yeh, S. Kenkel, J.-N. Liu, R. Bhargava, Fast infrared chemical imaging with a quantum cascade laser. *Anal. Chem.* **87**, 485–493 (2015).
3. F. Rosi, C. Miliani, R. Braun, R. Harig, D. Sali, B. G. Brunetti, A. Sgamellotti, Noninvasive analysis of paintings by mid-infrared hyperspectral imaging. *Angew. Chem. Int. Ed. Engl.* **52**, 5258–5261 (2013).
4. K. Ruxton, G. Robertson, W. Miller, G. P. A. Malcolm, G. T. Maker, Mid-infrared hyperspectral imaging for the detection of explosive compounds. *Proc. SPIE.* **8546** (2012).
5. S. Sugawara, Y. Nakayama, H. Taniguchi, I. Ishimaru, Wide-field mid-infrared hyperspectral imaging of adhesives using a bolometer camera. *Sci. Rep.* **7**, 12395 (2017).
6. R. Ostendorf, L. Butschek, S. Hugger, F. Fuchs, Q. Yang, J. Jarvis, C. Schilling, M. Rattunde, A. Merten, J. Grahmann, D. Boskovic, T. Tybussek, K. Rieblinger, J. Wagner, Recent advances and applications of external cavity-QCLs towards hyperspectral imaging for standoff detection and real-time spectroscopic sensing of chemicals. *Photonics* **3**, 28 (2016).
7. J. Meléndez, G. Guarnizo, Fast quantification of air pollutants by mid-infrared hyperspectral imaging and principal component analysis. *Sensors (Basel)* **21**, 2092 (2021).
8. C. I. Honniball, R. Wright, P. G. Lucey, Mid-Wave Infrared Hyperspectral Imaging of Kilauea's Halema'uma'u lava lake, American Geophysical Union. 01 December 2018.
9. R. Bhargava, Infrared spectroscopic imaging: The next generation. *Appl Spectrosc.* **66**, 1091–1120 (2012).
10. E. S. Lee, J. Y. Lee, High resolution cellular imaging with nonlinear optical infrared microscopy. *Opt. Express* **19**, 1378–1384 (2011).
11. P. D. Samolis, M. Y. Sander, Phase-sensitive lock-in detection for high-contrast mid-infrared photothermal imaging with sub-diffraction limited resolution. *Opt. Express* **27**, 2643–2655 (2019).
12. D. Zhang, C. Li, C. Zhang, M. N. Slipchenko, G. Eakins, J.-X. Cheng, Depth-resolved mid-infrared photothermal imaging of living cells and organisms with submicrometer spatial resolution. *Sci. Adv.* **2**, e1600521 (2016).
13. A. Hanninen, M. W. Shu, E. O. Potma, Hyperspectral imaging with laser-scanning sum-frequency generation microscopy. *Biomed. Opt. Express* **8**, 4230–4242 (2017).
14. A. M. Hanninen, R. C. Prince, R. Ramos, M. V. Plikus, E. O. Potma, High-resolution infrared imaging of biological samples with third-order sum-frequency generation microscopy. *Biomed. Opt. Express* **9**, 4807–4817 (2018).
15. J. K. Manattayil, L. K. AS, R. Biswas, H. Kim, V. Raghunathan, Focus-engineered sub-diffraction imaging in infrared-sensitive third-order sum frequency generation microscope. *Opt. Express* **30**, 25612–25626 (2022).
16. I. Kviatkovsky, H. M. Chrzanowski, E. G. Avery, H. Bartolomaeus, S. Ramelow, Microscopy with undetected photons in the mid-infrared. *Sci Adv.* **6**, eabd0264 (2020).
17. A. V. Paterova, S. M. Maniam, H. Yang, G. Grenci, L. A. Krivitsky, Hyperspectral infrared microscopy with visible light. *Sci. Adv.* **6**, eabd0460 (2020).
18. A. Barh, P. J. Rodrigo, L. Meng, C. Pedersen, P. Tidemand-Lichtenberg, Parametric upconversion imaging and its applications. *Adv. Opt. Photonics* **11**, 952–1019 (2019).
19. S. Junaid, J. Tomko, M. P. Semtsiv, J. Kischkat, W. T. Masselink, C. Pedersen, P. Tidemand-Lichtenberg, Mid-infrared upconversion based hyperspectral imaging. *Opt. Express* **26**, 2203–2211 (2018).
20. P. Tidemand-Lichtenberg, J. S. Dam, H. Andersen, L. Høgstedt, C. Pedersen, Mid-infrared upconversion spectroscopy. *J. Opt. Soc. Am. B* **33**, D28–D35 (2016).
21. S. Junaid, S. Chaitanya Kumar, M. Mathez, M. Hermes, N. Stone, N. Shepherd, M. Ebrahim-Zadeh, P. Tidemand-Lichtenberg, C. Pedersen, Video-rate, mid-infrared hyperspectral upconversion imaging. *Optica* **6**, 702–708 (2019).
22. D. A. Fishman, C. M. Cirloganu, S. Webster, L. A. Padilha, M. Monroe, D. J. Hagan, E. W. van Stryland, Sensitive mid-infrared detection in wide-bandgap semiconductors using extreme non-degenerate two-photon absorption. *Nat. Photon.* **5**, 561–565 (2011).
23. C. M. Cirloganu, L. A. Padilha, D. A. Fishman, S. Webster, D. J. Hagan, E. W. van Stryland, Extremely nondegenerate two-photon absorption in direct-gap semiconductors [Invited]. *Opt. Express* **19**, 22951–22960 (2011).
24. D. Hutchings, E. W. Van Stryland, Nondegenerate two-photon absorption in zinc blende semiconductors. *J. Opt. Soc. Am. B* **9**, 2065–2074 (1992).
25. D. Knez, A. M. Hanninen, R. C. Prince, E. O. Potma, D. A. Fishman, Infrared chemical imaging through non-degenerate two-photon absorption in silicon-based cameras. *Light Sci. Appl.* **9**, 125 (2020).
26. E. O. Potma, D. Knez, Y. Chen, Y. Davydova, A. Durkin, A. Fast, M. Balu, B. Norton-Baker, R. W. Martin, T. Baldacchini, D. A. Fishman, Rapid chemically selective 3D imaging in the mid-infrared. *Optica* **8**, 995–1002 (2021).
27. E. O. Potma, D. Knez, M. Ettenberg, M. Wizeman, H. Nguyen, T. Sudol, D. A. Fishman, High-speed 2D and 3D mid-IR imaging with an InGaAs camera. *APL Photonics* **6**, 096108 (2021).
28. E. T. J. Nibbering, D. A. Wiersma, K. Duppen, Ultrafast nonlinear spectroscopy with chirped optical pulses. *Phys. Rev. Lett.* **68**, 514–517 (1992).
29. T. Hellerer, A. M. K. Enejder, A. Zumbusch, Spectral focusing: High spectral resolution spectroscopy with broad-bandwidth laser pulses. *Appl. Phys. Lett.* **85**, 25–27 (2004).
30. M. Mohseni, C. Polzer, T. Hellerer, Resolution of spectral focusing in coherent Raman imaging. *Opt. Express* **26**, 10230–10241 (2018).
31. K. J. Kubarych, M. Joffre, A. Moore, N. Belabas, D. M. Jonas, Mid-infrared electric field characterization using a visible charge-coupled-device-based spectrometer. *Opt. Lett.* **30**, 1228–1230 (2005).
32. J. Zhu, T. Mathes, A. D. Stahl, J. T. M. Kennis, M. L. Groot, Ultrafast mid-infrared spectroscopy by chirped pulse upconversion in 1800-1000cm^{-1} region. *Opt. Express* **20**, 10562–10571 (2012).
33. C.-S. Liao, K.-C. Huang, W. Hong, A. J. Chen, C. Karanja, P. Wang, G. Eakins, J.-X. Cheng, Stimulated Raman spectroscopic imaging by microsecond delay-line tuning. *Optica* **3**, 1377–1380 (2016).
34. M. S. Alshaykh, C.-S. Liao, O. E. Sandoval, G. Gitzinger, N. Forget, D. E. Leaird, J.-X. Cheng, A. M. Weiner, High-speed stimulated hyperspectral Raman imaging using rapid acousto-optic delay lines. *Opt. Lett.* **42**, 1548–1551 (2017).
35. R. He, Z. Liu, Y. Xu, W. Huang, H. Ma, M. Ji, Stimulated Raman scatstering microscopy and spectroscopy with a rapid scanning optical delay line. *Opt. Lett.* **42**, 659–662 (2017).

Acknowledgments: D.A.F. thanks Y. Davydova for all the help and support. We thank the Laser Spectroscopy Labs. D.A.F. wants to dedicate this work to our dear friend Luke. **Funding:** E.O.P. acknowledges NIH R01GM132506. E.O.P. and D.A.F. acknowledge NIH R21GM141774. **Author contributions:** D.A.F. and E.O.P. conceived of the idea and supervised the study. D.K. and D.A.F. conducted all experiments and analyzed the data. D.K. performed chirp pulse modeling. B.W.T. helped with automation of the optical setup. A.C. conducted FTIR experiments. M.H.E. and H.N. provided the InGaAs camera and assisted with its use. D.A.F. polished the Si rod. D.A.F., E.O.P., and D.K. wrote the initial paper, and all authors took part in editing. **Competing interests:** The authors declare that they have no competing interests. **Data and materials availability:** All data needed to evaluate the conclusions in the paper are present in the paper and/or the Supplementary Materials.

Submitted 15 August 2022
Accepted 20 October 2022
Published 16 November 2022
10.1126/sciadv.ade4247